Importance of confined fields in near-field optical imaging of subwavelength objects

Christian Girard
Laboratoire de Physique Moléculaire, Unité Associée au Centre National de la Recherche Scientifique No. 772, Université de Franche Comté, F-25030 Besançon Cedex, France

Alain Dereux
Institute of Studies in Interfaces Sciences, Facultés Universitaires Notre Dame de la Paix, Rue de Bruxelles 61, B-5000 Namur, Belgium

Olivier J. F. Martin
Swiss Federal Institute of Technology, Eidgenössiche Technische Hochschule, Institute for Field Theory, Gloriastrasse 35 CH-8092, Zürich, Switzerland

Michel Devel
Laboratoire de Physique Moléculaire, Unité Associée au Centre National de la Recherche Scientifique No. 772, Université de Franche Comté, F-25030 Besançon Cedex, France
(Received 23 May 1994)

The detailed imaging process of subwavelength objects deposited on a planar surface is studied within the framework of a three-dimensional model of scanning near-field optical microscope. The model consists of a truncated pointed fiber approaching a planar surface on which a three-dimensional protrusion is deposited. For this geometry, Maxwell's equations are solved exactly by applying the field-susceptibility method in the direct space. The technique provides precise evaluations of the physically relevant near and far fields. In order to refine the understanding of the imaging process of subwavelength objects, we present simulated images of low-symmetry protrusions for two different modes of polarization and as a function of the approach distance. These simulations show clearly that subwavelength surface defects induce confined optical near-field distributions that are directly related to the shapes of the objects. We conclude that the central problem of near-field optical microscopy is the optimal detection of the confined fields that are set up by the objects themselves.

I. INTRODUCTION

Photon imaging of subwavelength three-dimensional objects requires the detection of nonradiative field components confined a few nanometers above the sample surface. Since 1984, numerous experimental devices have attempted to apply this concept in the range of visible wavelengths.[1] One class of devices involves subwavelength holes and protrusions.[2,3] Another one relies on pointed fibers for emitting or collecting the light beam.[4–8] Successful practical devices have demonstrated the correlation of subwavelength-resolved signals with various object properties such as shape, polarizability, or index of refraction, and have opened opportunities for the optical characterization of surfaces. Recently, the scanning plasmon near-field microscope reached the super-resolution of $\lambda/200$ on silver samples[9] by exploiting near-fields associated with resonance phenomena.

In spite of these experimental advances, the imaging process of the various scanning near-field optical microscope (SNOM) devices remains questionable. In particular, the relative importance of the probe properties (shape and material) and of the illumination mode is still not well established. The situation is complicated by the fact that this microscopy arose as a challenge to theoretical optics, since near-field optical effects are beyond the scope of common approximations. In order to guide the rapid experimental developments and to understand the contrast mechanisms involved in near-field optics (NFO), several theoretical approaches and simulations techniques have been proposed.[10–16] Van Labeke and Barchiesi recently reviewed various theoretical methods.[16] However, a rather limited number of these theoretical descriptions took into account the self-consistent coupling between the probe and the sample surface, so that most of the basic questions raised above remained unanswered. The few self-consistent studies[17–19] indicated that the individual structures lying on the surface distorted the near field established by the self-consistent optical interaction between the probe and sample. Nevertheless, these distortions of the electromagnetic near field turned out to be confined very close to the protrusions of the illuminated surface. The same simulations showed that even if the modifications of the electromagnetic near field in the SNOM junction were restricted to the region of the surface defects, they altered significantly the detected far field. Furthermore, these self-consistent computations demonstrated unambiguously that a realistic description of SNOM devices requires a very accurate determination of the near-field distribution inside the coupled probe-sample system in order to assess how the far-field cross sections are related to subwavelength structures.

In the spirit of these preliminary self-consistent studies,

0163-1829/94/50(19)/14467(7)/$06.00

this paper presents a detailed study of these local interactions when a thin SNOM tip is scanning subwavelength three-dimensional (3D) objects.[20] In order to refine the understanding of the imaging process of such surface profiles, we simulated images of protrusions of low symmetry for two different modes of polarization and as a function of the approach distance. In Sec. II, we define the geometry of a SNOM device and summarize the steps leading to the self-consistent integral equation. A numerical discretization procedure will be used to solve this equation numerically in direct space and to derive the field distribution inside the SNOM junction. In order to obtain some insight into the optical interaction between tip and sample, the image-object relation will be examined in Sec. III by giving sequences of gray scale images as a function of the approach distance.

II. THEORETICAL FRAMEWORK

A. Vector Lippmann-Schwinger equation with 3D objects

In the present section, we outline the underlying analytical framework for our numerical simulations. The principle of our method relies on the splitting into two parts of the physical system for which we are seeking a solution of the vectorial wave equation: a highly symmetrical reference system (in our case the perfect planar surface limiting the infinite homogeneous half-spaces considered in our application, Fig. 1) and a perturbation embedded in this reference system (for example the ensemble formed by a 3D defect lying on the perfect surface and the probing tip, Fig. 1). By perturbation we do not mean that its physical properties differ slightly from the reference system, but rather that the perturbation is spatially limited within the reference system.

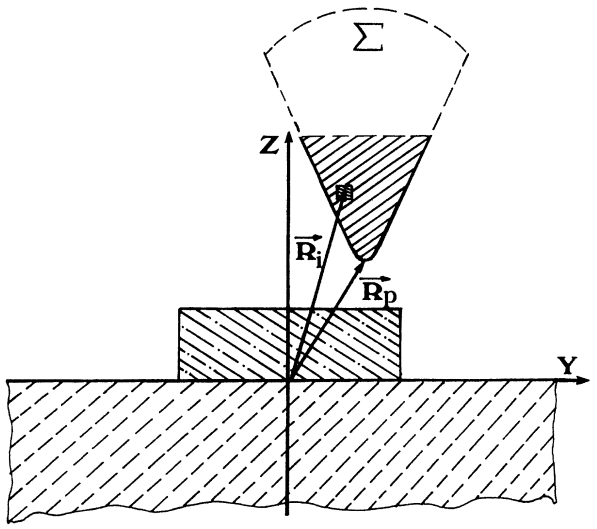

FIG. 1. Schematic illustration of a scanning probe device. The vector $\mathbf{R}_p=(X,Y,Z)$ defined the detector apex position, and $\mathbf{R}_i$ characterizes the location of a given volume element inside the probe tip. The shadowed zones including the surface defect and the tip extremity were treated by discretization in the Cartesian space.

Let $\mathbf{E}_0(\mathbf{r},\omega)$ be the known Fourier component of the incident field on the highly symmetrical system. In the presence of the perturbation (probing tip plus localized surface defect) the perturbed field $\mathbf{E}(\mathbf{r},\omega)$ obeys the following implicit Lippmann-Schwinger equation:[21]

$$\mathbf{E}(\mathbf{r},\omega)=\mathbf{E}_0(\mathbf{r},\omega)+\int \mathbf{S}(\mathbf{r},\mathbf{r}',\omega)\cdot\chi(\mathbf{r}',\omega)\cdot\mathbf{E}(\mathbf{r}',\omega)d\mathbf{r}' , \tag{1}$$

where $\mathbf{S}(\mathbf{r},\mathbf{r}',\omega)$ represents the field susceptibility of the reference system[20] (cf. Fig. 1), and $\chi(\mathbf{r}',\omega)$ is the linear susceptibility of the perturbation (localized defect plus probe tip). The first term of this self-consistent equation corresponds to the field in the absence of perturbation, whereas the second term gives the modification of the field due to the perturbation.

An approach based on the numerical solution of Eq. (1) turned out to be extremely powerful to investigate complex 3D systems,[20] and established the advantage of working in direct space rather than in reciprocal space. Indeed the treatment avoids the numerical difficulties associated with the poor convergence of the Fourier series involved in a reciprocal space description. Moreover, working in direct space allows us to consider arbitrary geometrical configurations.

In the upper half-space ($z\geq 0$), the second-rank tensor $\mathbf{S}(\mathbf{r},\mathbf{r}',\omega)$ is the sum of two contributions:

$$\mathbf{S}(\mathbf{r},\mathbf{r}',\omega)=\mathbf{S}_0(\mathbf{r},\mathbf{r}',\omega)+\mathbf{S}_s(\mathbf{r},\mathbf{r}',\omega) , \tag{2}$$

where the first term represents the field propagator in vacuum.[22] The presence of a surface at $z=0$ is described by the field susceptibility $\mathbf{S}_s(\mathbf{r},\mathbf{r}',\omega)$. The field susceptibility defined in (2) can be constructed by calculating the response field of the reference system to an arbitrary fluctuating dipole lying in its neighborhood.[22] In the particular case of a solid (dielectric or metallic) bounded by a perfectly planar surface, various theoretical methods were developed to obtain this response function. The analytical form of $\mathbf{S}(\mathbf{r},\mathbf{r}',\omega)$ depends on the nature of the surface under consideration. In the numerical work to be discussed in this paper, we used the analytical form of $\mathbf{S}(\mathbf{r},\mathbf{r}',\omega)$ which can be found in Ref. 22: Eqs. (23) and (24).

B. Near-field distribution inside the probe-sample system

In SNOM experimental setups, the main element is the tip of a dielectric stylus. The current trend is the use of monomode fibers for which the conical tip is obtained by different techniques such a chemical etching or pulling-heating processes.[4–8] In this subsection we consider the problem of such a pointed dielectric stylus facing a plane surface displaying a three-dimensional localized defect (cf. Fig. 1). In experimental devices, the probe and the sample always remain as two well-separated systems during a scan. Consequently the electric susceptibility $\chi(\mathbf{r},\omega)$ describing the linear-response properties of the perturbation can be written as the sum of two contribu-

tions associated with the probe and the object, respectively,

$$\chi(\mathbf{r},\omega)=\chi_{\rm pr}(\mathbf{r},\omega)+\chi_{\rm ob}(\mathbf{r},\omega) \ . \tag{3}$$

When the optical response properties of both the probe and the surface defect are assumed to be local, $\chi_{\rm pr}$ and $\chi_{\rm ob}$ can be expressed in terms of the bulk optical dielectric constants $\epsilon_{\rm pr}$ and $\epsilon_{\rm ob}$. One then has (with j standing for pr and ob)

$$\chi_j(\mathbf{r},\omega)=\frac{\epsilon_j(\omega)-1}{4\pi} \tag{4}$$

for all points $\mathbf{r}$ located inside the perturbation (probe plus surface defect), and

$$\chi_j(\mathbf{r},\omega)=0 \tag{5}$$

outside the perturbation.

From relations (4) and (5) the integral equation (1) can be expressed as follows:

$$\mathbf{E}(\mathbf{r},\omega)=\mathbf{E}_0(\mathbf{r},\omega)+\mathcal{E}_{\rm pr}(\mathbf{r},\omega)+\mathcal{E}_{\rm ob}(\mathbf{r},\omega) \ , \tag{6}$$

where

$$\mathcal{E}_j(\mathbf{r},\omega)=\frac{\epsilon_j(\omega)-1}{4\pi}\int_j \mathbf{S}(\mathbf{r},\mathbf{r}',\omega)\cdot\mathbf{E}(\mathbf{r}',\omega)d\mathbf{r}' \ . \tag{7}$$

In the expressions for $\mathcal{E}_{\rm pr}$ and $\mathcal{E}_{\rm ob}$, the two integrations have to be performed over the volume of the probe and the object, respectively. An essential advantage of the present description is provided by the spatial localization of the perturbation which allows us to solve exactly the self-consistent equation (6). In fact, the solution of this implicit integral equation can be obtained by discretizing the spatial region occupied by the perturbation. Let us label the set of grid points inside the probe by $\{\mathbf{R}_i\}$ and the set of grid points used to treat the surface defect by $\{R_j\}$. After spatial discretization, the structure of Eq. (6) is

$$\begin{aligned}\mathbf{E}(\mathbf{r},\omega)=&\mathbf{E}_0(\mathbf{r},\omega)\\&+\frac{\epsilon_{\rm pr}(\omega)-1}{4\pi}\sum_{i=1}^{n} W_i^{\rm pr}\mathbf{S}(\mathbf{r},\mathbf{R}_i,\omega)\cdot\mathbf{E}(\mathbf{R}_i,\omega)\\&+\frac{\epsilon_{\rm ob}(\omega)-1}{4\pi}\sum_{j=1}^{m} W_j^{\rm ob}\mathbf{S}(\mathbf{r},\mathbf{R}_j,\omega)\cdot\mathbf{E}(\mathbf{R}_j,\omega) \ ,\end{aligned} \tag{8}$$

where $W_i^{\rm pr}$ and $W_j^{\rm ob}$ represent the volume of the discretized elements inside the tip apex and the surface defect.

The spatial localization of the perturbation means that both indices n and m remain finite, so that the resulting matrix equations can be solved by standard procedures of linear algebra:

$$\begin{aligned}\mathbf{E}(\mathbf{R}_k,\omega)=&\mathbf{E}_0(\mathbf{R}_k,\omega)\\&+\sum_{l=1}^{n+m}\mathbf{S}(\mathbf{R}_k,\mathbf{R}_l,\omega)\cdot\alpha_l(\omega)\cdot\mathbf{E}(\mathbf{R}_l,\omega) \ .\end{aligned} \tag{9}$$

In this last equation the quantity $\alpha_l(\omega)$ has the dimension of a dynamical polarizability, and changes its value according to the index l:

$$\alpha_l(\omega)=\left\{\frac{\epsilon_{\rm pr}(\omega)-1}{4\pi}\right\}W_l^{\rm pr} \quad \text{if } (1\le l\le n) \tag{10}$$

and

$$\alpha_l(\omega)=\left\{\frac{\epsilon_{\rm ob}(\omega)-1}{4\pi}\right\}W_l^{\rm ob} \quad \text{if } (n+1\le l\le n+m) \ . \tag{11}$$

We note that the procedure avoids matching boundary conditions. The latter are in fact implicitly guaranteed by the self-consistency of the original integral equation (1). The only approximation of the technique lies in the use of the spatial discretization; the density of the grid is arbitrarily adjustable.[11,12,20]

Note that the size of the matrix associated with the discretized Eq. (9) grows with the volume of the perturbation. Recently, we proposed a numerical scheme based on the parallel resolution of Lippmann-Schwinger and Dyson equations in order to restrict the numerical effort to the physically meaningful quantities.[23]

C. Intensity collected by the tip

In SNOM devices the use of a pointed detector allows the convertion of the nonradiative fields concentrated near the surface irregularities into radiative fields detectable in the far-field region. The amount of optical energy converted by such devices depends mainly on the shape and size of the region of interaction with the confined

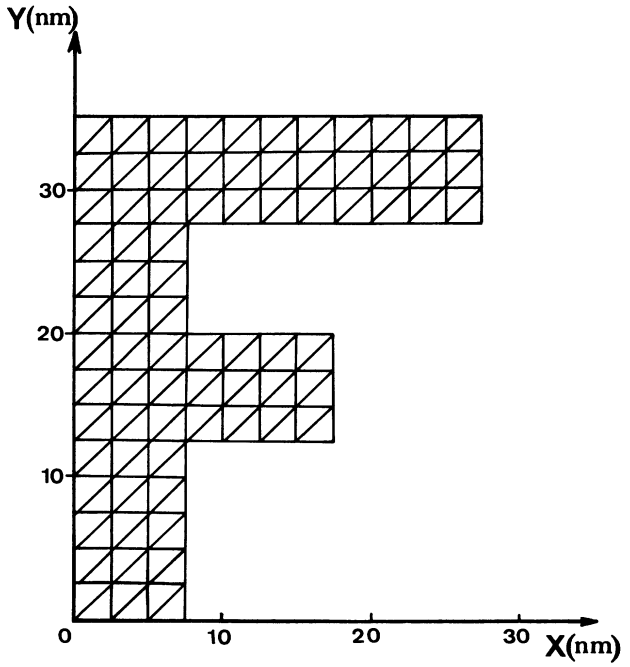

FIG. 2. Geometry of the three-dimensional pattern used in the first simulation presented in Sec. III (intensity growing from black to white). We have considered a letter F of 7.5 nm in thickness and 35 nm in height with an optical index of refraction of 1.5, identical to that of the substrate. In the calculation, the pattern is discretized with 228 cubic meshes of size 2.5 nm.

fields. It is also very sensitive to both the object parameters and the illumination conditions (internal total reflection, angle of illumination, external illumination, etc). The conversion mechanism can be analyzed theoretically using the theory described above. In fact, knowledge of the effective field distribution inside the perturbation is sufficient to describe the far-field $\mathbf{E}_{\text{far}}$ crossing a surface Σ located in the wave zone of the dielectric stylus (cf. Fig. 1). We have the result

$$\mathbf{E}_{\text{far}}(\mathbf{R}+\mathbf{r}_0,\omega)=\sum_{k=1}^{n+m}\mathbf{S}(\mathbf{R}+\mathbf{r}_0,\mathbf{R}_k,\omega)\cdot\alpha_k(\omega)\cdot\mathbf{E}(\mathbf{R}_k,\omega)\ , \tag{12}$$

where $\mathbf{R}_p$ defines the location of the tip apex with respect to an absolute reference frame, and the vector $\mathbf{r}_0$ represents the position of a point of the Σ surface with respect to the apex of the detector.[24] By using an asymptotic form of the propagator $\mathbf{S}$ in the far-field range, it is possible to describe regions far away from the perturbation. Finally, numerical integration of the Poynting vector associated with $\mathbf{E}_{\text{far}}(\mathbf{R}_p+r_0,\omega)$ on the surface of the cross section Σ of the probe leads to the energy flux across that section and hence to the detected intensity $I(\mathbf{R}_p,\omega)$ which is the relevant observable in experiments.

III. SCANNING OVER SUBWAVELENGTH 3D OBJECTS

The two relations (9) and (12) defined in the previous sections are general since they account for the real profile of both the tip apex and the object. From these equations it is possible to calculate the signal $I(\mathbf{R}_p,\omega)$ and to simulate, by scanning the detector, SNOM images. Both quasipoint and spatially extended probe tips will be considered in our calculations.

A. Imaging with quasipoint probe tips

Our first example considers the problem of near-field image calculations of a three-dimensional dielectric subwavelength object lying on a perfectly flat glass surface (the reference system). In order to minimize the tip-sample coupling we have considered, in a first step, a quasipoint tip apex (2.5-nm curvature at its extremity and 10-nm height). The three-dimensional object used in this first application is a letter **F** of optical index 1.5, thickness 7.5 nm, and height 35 nm (cf. Fig. 2). We consider the internal total reflection [STOM/PSTM (STOM is scanning tunneling optical microscopy and PSTM is photon scanning tunneling optical microscopy] configuration described in Refs. 4–8 with an incident wavelength $\lambda=632$ nm. In such a configuration, the zeroth-order field $\mathbf{E}_0(\mathbf{r},\omega)$ is the evanescent wave created by total reflection at the surface ($z=0$). For the computation, we

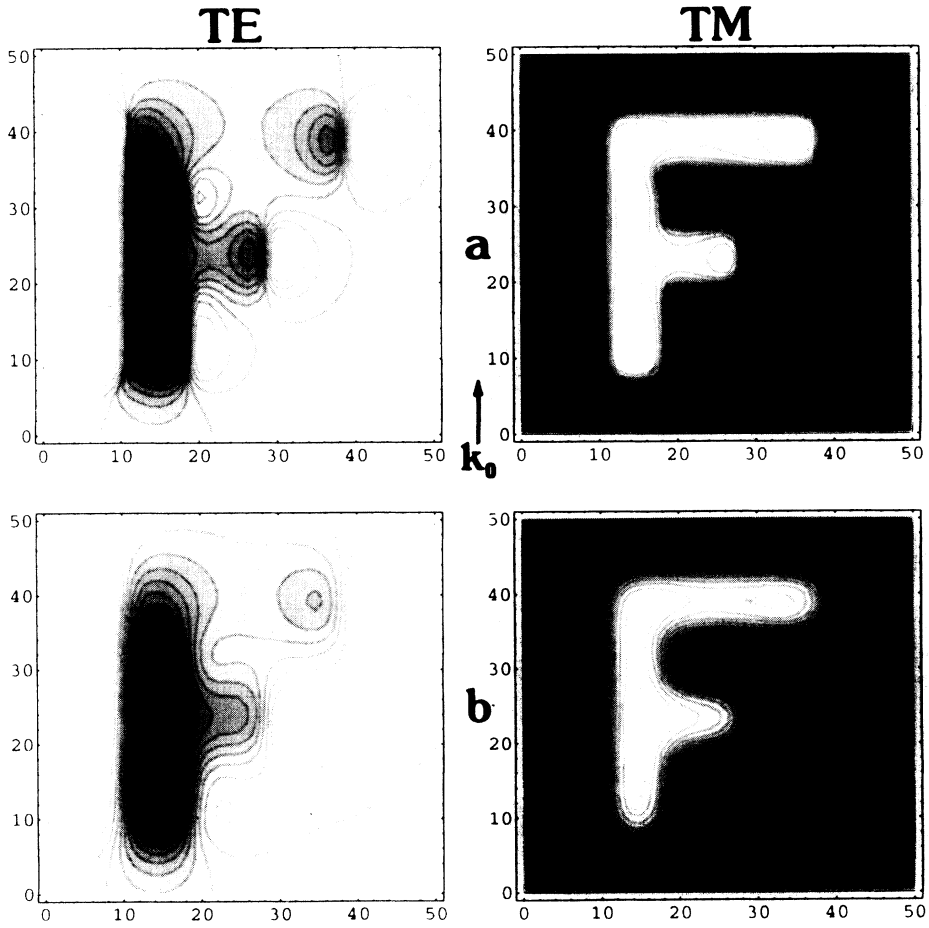

FIG. 3. A sequence of gray scale images corresponding to the 3D object described in Fig. 2. The evolution of the image is given as a function of the approach distance for two different modes of the external polarization (transverse electric and transverse magnetic). The sample is lit in internal total reflection corresponding to the so-called STOM/PSTM configuration, and the incident wave vector is parallel to the OY axis (black arrow on the figures). The intensity $I(\mathbf{R}_p)$ collected by the probe was calculated in a plane parallel to the reference system at a distance Z from the plane surface. The scanned area is (50×50) nm^2 and the incident wavelength is 632 nm. This simulation was performed with a quasipunctual tip apex (2.5-nm curvature at its extremity and 10-nm height). The vector $\mathbf{k}_0$ represents the projection of the incident wave vector in the plane (XOY). (a) $Z=10$ nm. (b) $Z=15$ nm. (c) $Z=20$ nm. (d) $Z=40$ nm.

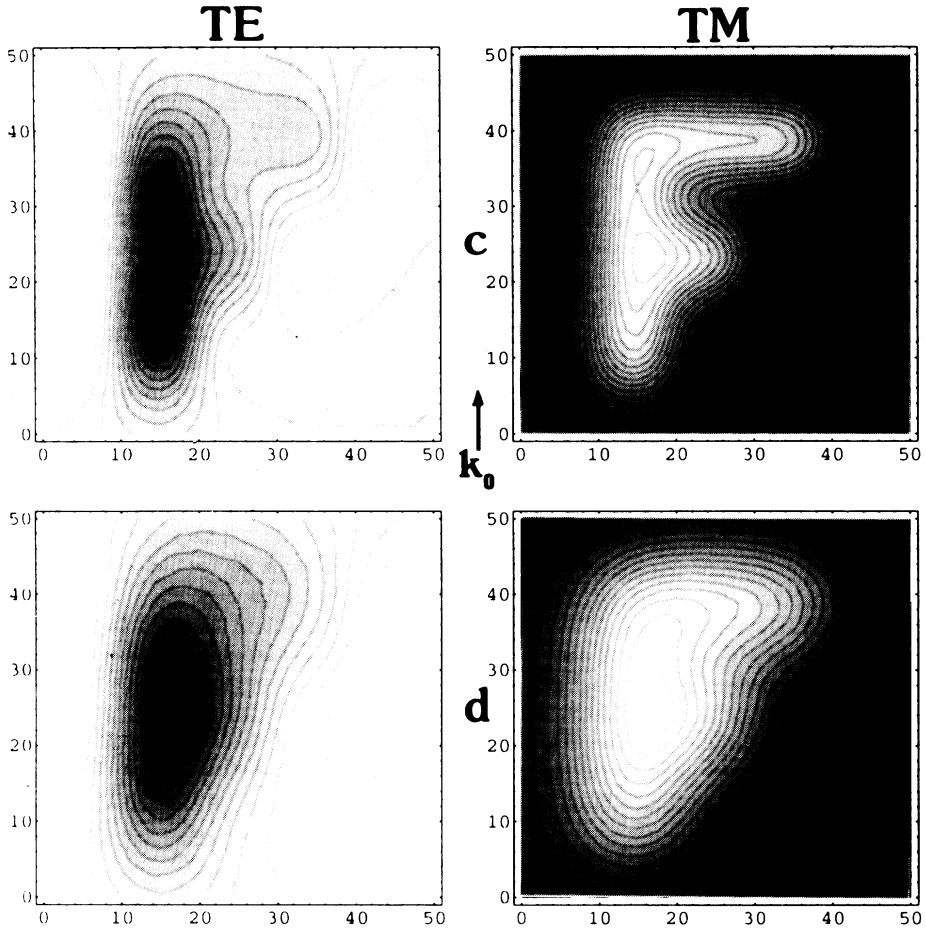

FIG. 3. (*Continued*).

formed a Cartesian discretization grid consisting of three consecutive layers of 76 cubic elements of size 2.5 nm.

Figure 3 displays a sequence of gray scale images of this object calculated at constant distance from the reference system. In these images the object induces strong-field confinement for both TM and TE polarizations. In the TM mode, the defect induces a well-localized increase of the near-field distribution directly related to the shape of the object. The image-object relation of subwavelength structures appears to be optimal when the incident electric field is perpendicular to the interface plane. A different feature occurs in the TE image in which the incident field polarization is parallel to the surface of the reference system. In this case, some spatial region located above the object appears in reversed contrast relative to the object relief. The spatial extension of the contrast reversal region is fixed by the size of the localized surface corrugation. Moreover, in the direction parallel to the incident beam, enhanced confinement is found above the edges of the object. Such an electromagnetic confinement could explain the high-resolution obtained by Courjon, Bainier, and Spajer by working in the TE mode when recording low relief objects[25] (5 nm in thickness).

The phenomenon of contrast reversal can be explained simply by examining the sign of the dominating short-range term $\mathbf{S}_0^{(\mathrm{sh})}(\mathbf{r}_a,\mathbf{r}_0)$ composing the free space propagator $\mathbf{S}_0$ [cf. Eq. (2) and Ref. 10]. In fact when a small sample of the very tip (located at $\mathbf{r}_0$) passes over an elementary sample of the surface defect (located at $\mathbf{r}_a$), $\mathbf{S}_0^{(\mathrm{sh})}(\mathbf{r}_0-\mathbf{r}_a)$ takes the form, with $\mathbf{r}_0-\mathbf{r}_a=(0,0,z_0-z_a)$,

$$\mathbf{S}_0^{(\mathrm{sh})}(\mathbf{r}_0-\mathbf{r}_a)=\begin{bmatrix}-[z_0-z_a]^{-3} & 0 & 0\\ 0 & -[z_0-z_a]^{-3} & 0\\ 0 & 0 & 2[z_0-z_a]^{-3}\end{bmatrix}. \tag{13}$$

The near field generated inside the very tip deduced from Eq. (1) can then be approximated by

$$\mathbf{E}(\mathbf{r}_0,\omega)\simeq\mathbf{E}_0(\mathbf{r}_0,\omega)+\alpha(\omega)\mathbf{S}_0^{\mathrm{sh}}(\mathbf{r}_0-\mathbf{r}_a,\omega)\cdot\mathbf{E}_0(\mathbf{r}',\omega)\ . \tag{14}$$

As a consequence of the minus sign in the first row of Eq. (13), the second term of Eq. (14) appears in phase opposition with the evanescent field in the TE mode:

$$\mathbf{E}_0(\mathbf{r}_0,\omega)=(E_0(\mathbf{r}_0,\omega),0,0)\ , \tag{15}$$

which results in a near-field decrease in the immediate

proximity of the sample. In the TM mode, the z component dominates and imposes a positive sign on $S_0^{(sh)}$. Note that a similar behavior has been observed in the framework of the diffraction theory described in Ref. 26. This contrast reversal may appear more familiar when considering depolarization effects. In the TE mode, the incident electric field is oriented along the x direction, so that the finite size of the object induces strong depolarization effects which reduce the intensity of the electric field inside the object. In the TM mode, the incident electric field has a vertical component (along z) and a horizontal component (along y) which interact with each other inside the objects. As indicated by Eq. (13), the z component dominates at short distances, so that scanning in a detection plane above the object is more sensitive to the vertical depolarization which masks the horizontal depolarization effect.

B. Imaging with extended probe tips

In a practical STOM (or PSTM) configuration, the pointed fiber is brought near the sample in region where the magnitude of the evanescent field is significantly intense. The evanescent illumination reduces the amount of stray light entering the taper laterally so that the part of the detector which is located outside the decay range of the surface near field contributes weakly to multiple-scattering effects between the tip and sample. A fairly good approximation then allows us to limit the height of the pointed fiber to the decay length η of the evanescent field. η reaches about 100 nm if the evanescent field is generated by a plane wave which is incident slightly above the critical angle for total reflection. In the analysis of the imaging process with extended probe tips, we therefore restricted the height of the conical probe tip to 100 nm. The tip apex had a realistic curvature radius of 15 nm. This truncated detector was then discretized on a Cartesian grid by stacking layers of meshes in a close-packed arrangement. The detector described above was brought above a T-shaped three-dimensional object engraved on a transparent glass substrate. This T was 5 nm thick and 70 nm long. Many of the features found in the case of a quasipoint detector are recovered. In particular, depolarization effects follow the same trends as observed for a quasipoint probe. From our simulations we conclude that the sharp resolution of the object is still possible with an extended detector. The loss of quality related to the growing size of the detector may be appreciated by comparing Figs. 3(a) and 3(b) with Figs. 4(a) and 4(b). For an approach height of 10 nm, the quasipoint probe tip provides a sharper image than the extended tip. But the extended probe tip can recover a sharp image by coming 5 nm closer to the sample.

We tested the stability of the image profile versus the number of layers used to discretize the conical tip. Increasing the number of layers from five to seven did not

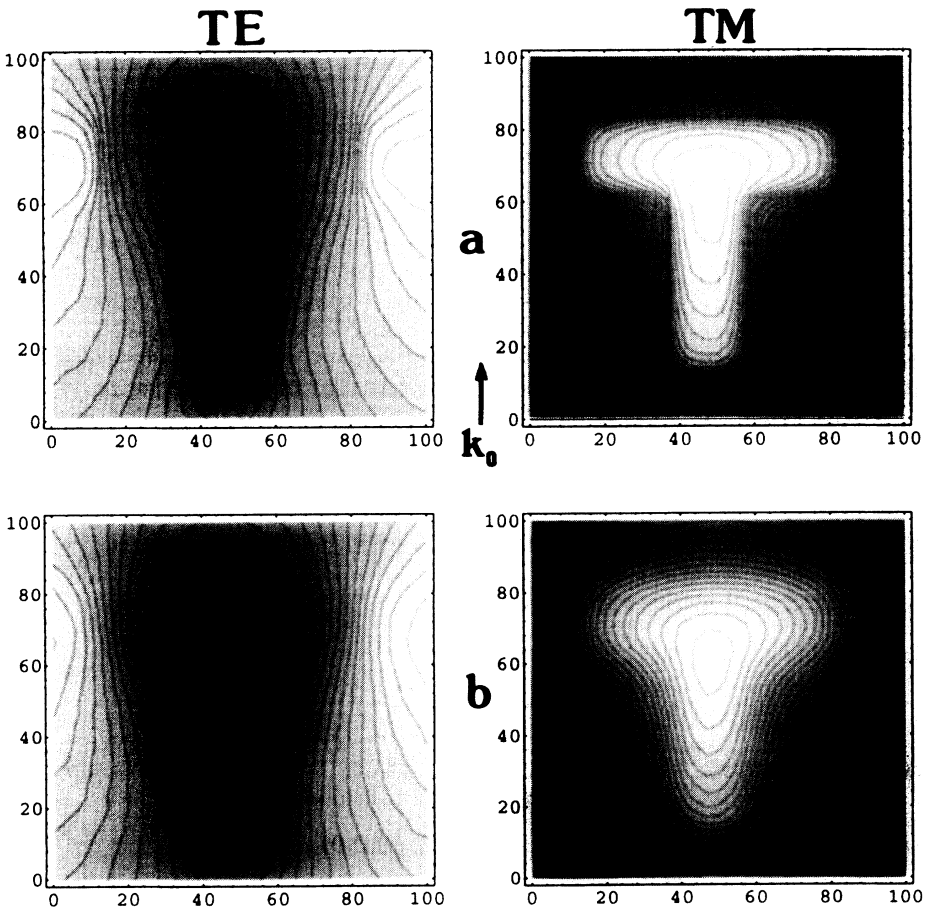

FIG. 4. Simulated images of a letter T engraved on a transparent substrate of optical index of refraction 1.5. The thickness and height of this 3D pattern are 5 and 70 nm, respectively. The calculation was applied by using a probe tip of realistic size discretized with 54 cells positioned in a closed packed arrangement (15-nm curvature at its extremity, 100-nm nanometer height). The vector $\mathbf{k}_0$ represents the projection of the incident wave vector on the plane (XOY). Two different approach distances were considered: (a) $Z=6$ nm, and (b) $Z=10$ nm.

affect the lateral variation of the detected intensity but contributed to the signal background. In other words, extending the tip further changed the absolute value of the intensity but not the relative definition of the image. The confined field responsible for the observed image is thus set up by the objects themselves. How to couple the near field associated to the objects with the radiative far field is the basic question of tip design, which is important to achieve a convenient detection level by reducing the noise.

IV. CONCLUSION

We have presented some numerical applications relevant to the principles and technology of near-field optical microscopy. Our direct-space approach is based on a general theoretical framework which handles the self-consistent electromagnetic field arising from scattering by three-dimensional objects and gives access to observables which are relevant experimentally, such as the light intensity collected by a NFO probing system (a STOM/PSTM tip, for example). We have used this model to investigate the imaging properties, in a STOM/PSTM configuration, of subwavelength three-dimensional objects lying on a surface. Our results show that a strong confinement of the electromagnetic field in the vicinity of these three-dimensional objects is responsible for the extraordinary resolution observed experimentally. The topography of this confined field, and therefore the collected image, depend strongly on the polarization of the evanescent field used for illuminating the object. When the electric field is parallel to the surface supporting the object (TE field), a strong-field confinement arises along the object interfaces orthogonal to the field, and the image-object relation emphasizes the outline of the object; different orientations of the incident field highlight different sides of the object. When a TM field is used, the field pattern reproduces the shape of the object. In this situation, the image emphasizes the entire volume of the object and is independent of the orientation of the incident field. This explains the high sensitivity of the experimental images to the operating polarization mode. The influence of the detector geometry, and of the probing distance on image formation has also been considered. In particular we have shown that the coupling between the apex of the detector and the object plays a principal role in the imaging process: beyond a given detector dimension, the image remains unchanged. We found that the loss of resolution associated with an extended tip may be counterbalanced by approaching the probe tip closer to the sample. This property could orientate near-field optical instrumentation to improve the tip-sample control in order to optimize the detection of the confined field set up by the objects themselves.

ACKNOWLEDGMENTS

This work was performed in the framework of the Human Capital and Mobility Programm *Near-Field Optics for Nanoscale Science and Technology* initiated by the European Community. The authors have benefited from useful discussions with D. Courjon, D. W. Pohl, J. P. Vigneron, and M. Spajer, and from careful proofreading of the manuscript by J. Killingbeck.

[1]For a historical presentation of near-field optics, see for example, D. W. Pohl in *Near Field Optics,* Vol. 242 of *NATO Advanced Study Institute, Series E: Applied Sciences,* edited by D. W. Pohl and D. Courjon (Kluwer, Dordrecht, 1993), pp. 1–5.

[2]E. Betzig, J. K. Trautman, T. D. Harris, J. S. Weiner, and R. L. Kostelak, Science **251**, 1468 (1991), and references therein.

[3]K. Lieberman and A. Lewis, Ultramicroscopy **42-44**, 399 (1991).

[4]R. Reddick, R. J. Warmack, and T. J. Ferrell, Phys. Rev. B **39**, 767 (1989).

[5]D. Courjon, K. Sarayeddine, and M. Spajer, Opt. Commun. **71**, 23 (1989).

[6]N. F. Van Hulst, F. B. Segering, and B. Bolger, Opt. Commun. **87**, 212 (1992).

[7]T. L. Ferrell, S. L. Sharp, and R. J. Warmack, Ultramicroscopy **42-44**, 408 (1991).

[8]F. de Fornel, L. Salomon, P. Adam, E. Bourillot, J. P. Goudonnet, and M. Neviere, Ultramicroscopy **42-44**, 422 (1992).

[9]M. Specht, J. D. Pedarnig W. M. Heckl, and T. W. Hansch, Phys. Rev. Lett. **68**, 476 (1992).

[10]C. Girard and D. Courjon, Phys. Rev. B **42**, 9340 (1990).

[11]A. Dereux, Ph.D. thesis, Faculté Universitaire N. D. de la Paix, NAMUR, Belgium, 1991.

[12]A. Dereux, J. P. Vigneron, Ph. Lambin, and A. A. Lucas, Physica B **175**, 65 (1991).

[13]A. Roberts, J. Appl. Phys. **70**, 4045 (1991).

[14]D. Van Labeke and D. Barchiesi, J. Opt. Soc. Am. A **9**, 732 (1992).

[15]S. Berntsen, E. Bozhevolnaya, and S. Bozhevolnyi, J. Opt. Soc. Am. A **10**, 878 (1993).

[16]D. Van Labeke and D. Barchiesi, in *Near Field Optics* (Ref. 1), pp. 157–178.

[17]A. Dereux and D. W. Pohl, in *Near Field Optics* (Ref. 1), pp. 189–198.

[18]A. Castiaux, A. Dereux, J. P. Vigneron, C. Girard, and O. J. F. Martin, Ultramicroscopy (to be published).

[19]L. Novotny, D. W. Pohl, and P. Regli, Ultramicroscopy (to be published).

[20]C. Girard, A. Dereux, and O. J. F. Martin, Phys. Rev. B **49**, 13 872 (1994).

[21]E. N. Economou, *Green's Functions in Quantum Physics,* 2nd ed. (Springer, Berlin, 1983).

[22]C. Girard and X. Bouju, J. Chem. Phys. **95**, 2056 (1991).

[23]O. J. F. Martin, A. Dereux, and C. Girard, J. Opt. Soc. Am. A **11**, 1073 (1994).

[24]C. Girard and A. Dereux, Phys. Rev. B **49**, 11 344 (1994).

[25]D. Courjon, C. Bainier, and M. Spajer, J. Vac. Sci. Technol. B **10**, 2436 (1992).

[26]D. Barchiesi, Ph.D. thesis, Université de Besançon, France, 1993.

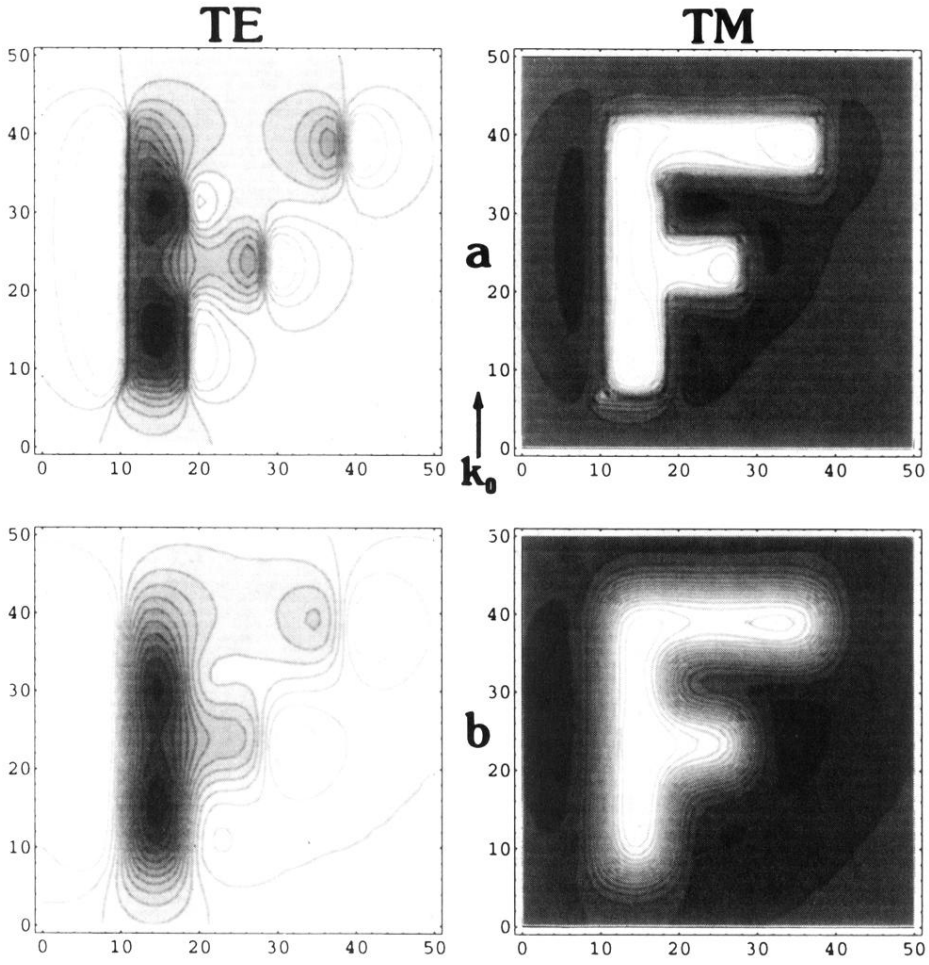

FIG. 3. A sequence of gray scale images corresponding to the 3D object described in Fig. 2. The evolution of the image is given as a function of the approach distance for two different modes of the external polarization (transverse electric and transverse magnetic). The sample is lit in internal total reflection corresponding to the so-called STOM/PSTM configuration, and the incident wave vector is parallel to the OY axis (black arrow on the figures). The intensity $I(\mathbf{R}_p)$ collected by the probe was calculated in a plane parallel to the reference system at a distance Z from the plane surface. The scanned area is (50×50) nm^2 and the incident wavelength is 632 nm. This simulation was performed with a quasipunctual tip apex (2.5-nm curvature at its extremity and 10-nm height). The vector $\mathbf{k}_0$ represents the projection of the incident wave vector in the plane (XOY). (a) $Z=10$ nm. (b) $Z=15$ nm. (c) $Z=20$ nm. (d) $Z=40$ nm.

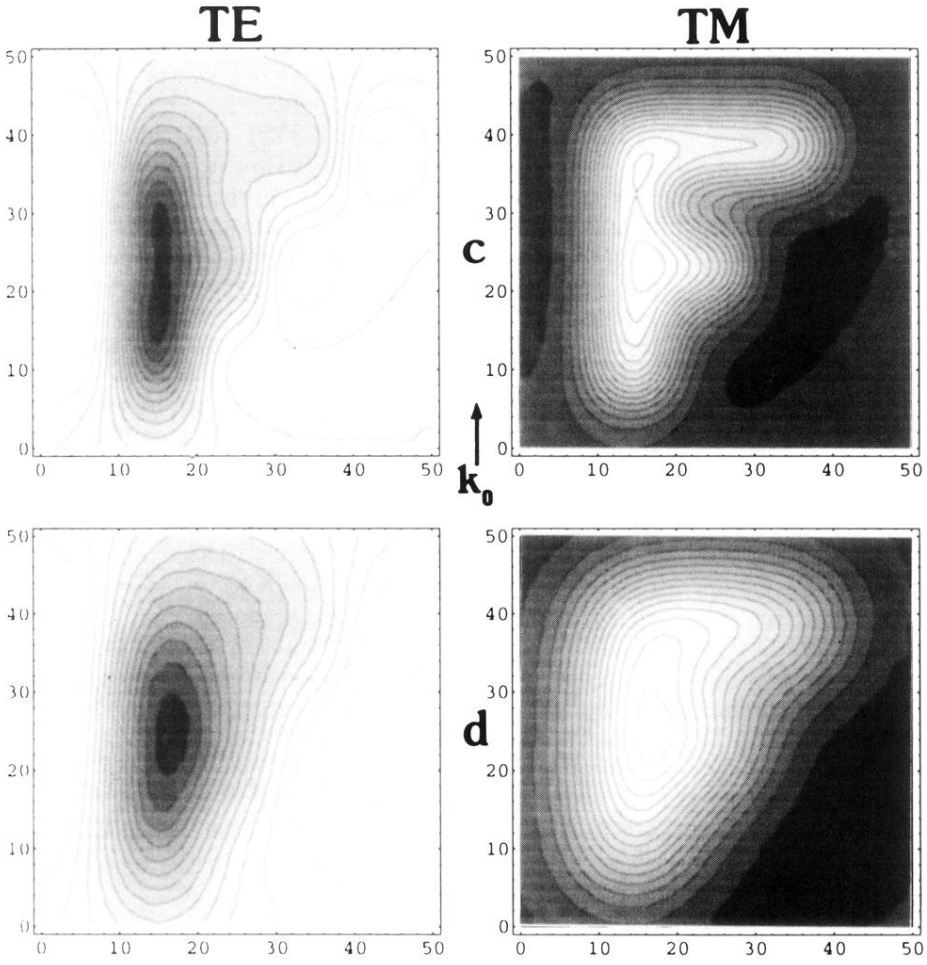

FIG. 3. (*Continued*).

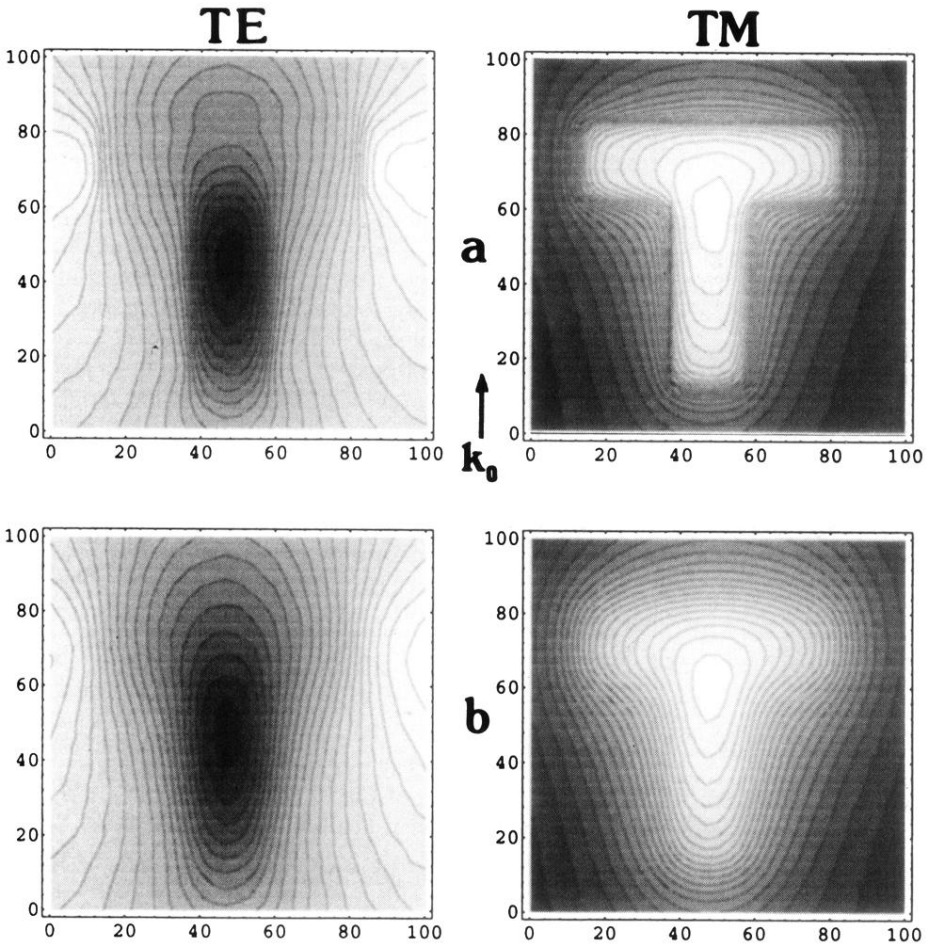

FIG. 4. Simulated images of a letter **T** engraved on a transparent substrate of optical index of refraction 1.5. The thickness and height of this 3D pattern are 5 and 70 nm, respectively. The calculation was applied by using a probe tip of realistic size discretized with 54 cells positioned in a closed packed arrangement (15-nm curvature at its extremity, 100-nm nanometer height). The vector $\mathbf{k}_0$ represents the projection of the incident wave vector on the plane (XOY). Two different approach distances were considered: (a) $Z = 6$ nm, and (b) $Z = 10$ nm.